

**Key Points:**

- A cloud model is used for dehydration of air parcels entering the stratosphere
- Water and cloud simulations are in agreement with MLS and CALIOP observations
- Convection is responsible for > 60% cloud in the tropical upper troposphere

**Correspondence to:**

M. R. Schoeberl,  
mark.schoeberl@mac.com

**Citation:**

Schoeberl M. R., A. E. Dessler, T. Wang, M. A. Avery, and E. J. Jensen (2014), Cloud formation, convection, and stratospheric dehydration, *Earth and Space Science*, 1, 1–17, doi:10.1002/2014EA000014.

Received 13 AUG 2014

Accepted 22 OCT 2014

Accepted article online 10 NOV 2014

Published online 11 DEC 2014

## Cloud formation, convection, and stratospheric dehydration

**Mark R. Schoeberl<sup>1</sup>, Andrew E. Dessler<sup>2</sup>, Tao Wang<sup>2,3</sup>, Melody A. Avery<sup>4</sup>, and Eric J. Jensen<sup>5</sup>**

<sup>1</sup>Science and Technology Corporation, Columbia, Maryland, USA, <sup>2</sup>Atmospheric Sciences Department, Texas A&M University, College Station, Texas, USA, <sup>3</sup>NASA Jet Propulsion Laboratory/California Institute of Technology, Pasadena, California, USA, <sup>4</sup>NASA Langley Research Center, Hampton, Virginia, USA, <sup>5</sup>NASA Ames Research Center, Moffett Field, California, USA

**Abstract** Using the Modern-Era Retrospective Analysis for Research and Applications (MERRA) reanalysis winds, temperatures, and anvil cloud ice, we use our domain-filling, forward trajectory model combined with a new cloud module to show that convective transport of saturated air and ice to altitudes below the tropopause has a significant impact on stratospheric water vapor and upper tropospheric clouds. We find that including cloud microphysical processes (rather than assuming that parcel water vapor never exceeds saturation) increases the lower stratospheric average  $H_2O$  by 10–20%. Our model-computed cloud fraction shows reasonably good agreement with tropical upper troposphere (TUT) cloud frequency observed by the Cloud-Aerosol Lidar with Orthogonal Polarization (CALIOP) instrument in boreal winter with poorer agreement in summer. Our results suggest that over 40% of TUT cirrus is due to convection, and it is the saturated air from convection rather than injected cloud ice that primarily contributes to this increase. Convection can add up to 13% more water to the stratosphere. With just convective hydration (convection adds vapor up to saturation), the global lower stratospheric modeled water vapor is close to Microwave Limb Sounder observations. Adding convectively injected ice increases the modeled water vapor to ~8% over observations. Improving the representation of MERRA tropopause temperatures fields reduces stratospheric water vapor by ~4%.

### 1. Introduction

Stratospheric water vapor ( $H_2O$ ) is primarily determined by large-scale troposphere-to-stratosphere transport in the tropics and the oxidation of methane. Air parcels moving upward into the tropical stratosphere pass through the cold point where formation and sedimentation of ice dehydrates the air [e.g., Fueglistaler *et al.*, 2009; Randel and Jensen, 2013, and references therein]. This basic theory is supported by observations such as the low-entry water vapor mixing ratios [Kley *et al.*, 1982; Kelly *et al.*, 1993; Dessler, 1998], the coherent variation of tropopause water vapor and temperature [Mote *et al.*, 1996; Randel *et al.*, 2006; Schoeberl *et al.*, 2008; Ueyama *et al.*, 2014], and the extensive cirrus clouds observed near the tropical tropopause [e.g., Wang *et al.*, 1996; Winker and Trepte, 1998; Dessler *et al.*, 2006; Wang and Dessler, 2012; Massie *et al.*, 2013].

Trajectory models have demonstrated success at simulating many aspects of stratospheric  $H_2O$  [e.g., Fueglistaler *et al.*, 2005; Schoeberl and Dessler, 2011, hereafter SD11; Schoeberl *et al.*, 2012, hereafter S12; Schoeberl *et al.*, 2013, hereafter S13; Ueyama *et al.*, 2014]. In the SD11 forward domain-filling trajectory model, winds determine the parcel motion and temperature determines the  $H_2O$  content through instant adjustment of the parcel water vapor to not exceed predefined saturation limit. The assumption in this formulation is that any ice that forms quickly falls to lower atmospheric layers. We refer to this adjustment as instantaneous dehydration (ID).

Air parcels moving slowly upward across the tropopause will have their water vapor concentration fixed as they pass through the cold point. However, convective systems can bypass the cold point and deposit ice directly into the lower stratosphere. Hydration through convection was parameterized in SD11 through a system described by Dessler *et al.* [2007]. In that system, parcels coincident with convection were set to the local saturation mixing ratio. Methane oxidation can also add water to the air parcel, but this process is unimportant in the lower tropical stratosphere where methane oxidation rates are slow (SD11).

In SD11 and S12, we compared the modeled stratospheric water vapor to Microwave Limb Sounder (MLS) observations. These papers identified a number of processes that controlled stratospheric water vapor. These processes include the following: (1) the level of supersaturation permitted before ID, (2) the level of convective penetration into the tropical tropopause layer (TTL), and (3) the role of short timescale and small spatial-scale temperature oscillations produced by atmospheric waves—waves not resolved by the coarser time and spatial resolution of the reanalysis. For example, in our model, increasing the level of saturation

This is an open access article under the terms of the Creative Commons Attribution-NonCommercial-NoDerivs License, which permits use and distribution in any medium, provided the original work is properly cited, the use is non-commercial and no modifications or adaptations are made.

before ice is formed (say from 100% to 120% relative humidity) increases stratospheric water vapor. Recent results from aircraft campaigns [Jensen *et al.*, 2013] suggest that water vapor concentration routinely exceeds supersaturation if there are only a few ice crystals present. Likewise, changing the detrainment level of convective ice also changes stratospheric water vapor (higher detrainment altitudes increase water [see also Dessler *et al.*, 2007]), and increasing the amplitude of gravity waves will reduce stratospheric water through enhanced dehydration due to colder temperatures caused by waves.

The purpose of this work is to try and further reduce the uncertainty and constrain the parameterizations in the trajectory based water vapor models. Our first change is to modify how the trajectory model handles dehydration. In our previous work (and in most trajectory analyses), it is assumed that when the parcel exceeds saturation, a condensate forms and falls out of the parcel. In actuality, when a parcel saturates, complex processes such as hydrometeor formation, growth, sublimation, and gravitational settling are initiated [e.g., Jensen and Pfister, 2004]. These processes necessarily have an impact on the evolution of the parcel water vapor and stratospheric hydration. To simulate cloud processes, we use a simplified cloud model (CM) based on the approach of Fueglistaler and Baker [2006], hereafter FB06. To validate our CM, we exploit cirrus cloud observations, which provide important constraints on the condensation and dehydration process. Cirrus observed in the tropical tropopause layer (TTL) comes from two sources: (1) in situ stratiform cloud formation when air is uplifted, cools, and the relative humidity exceeds the condensation threshold and (2) ice from deep convection (anvil formation and blow off). As noted above, convective injection of ice above the cold point tropopause adds water directly to the stratosphere [Smith *et al.*, 2006; Dessler *et al.*, 2007]. Observational support for deep convective modification of stratospheric water vapor comes directly from aircraft measurements [Corti *et al.*, 2008; Schiller *et al.*, 2009] and measurements of stratospheric HDO that exceed Rayleigh fractionation values [Moyer *et al.*, 1996; Keith, 2000; Johnson *et al.*, 2001; Dessler and Sherwood, 2003; Dessler *et al.*, 2007].

The second model change applies to the parameterization of convection. In SD11 we used an outgoing longwave radiation (OLR)-based climatological scheme to account for convective occurrences. In that scheme MLS ice observations are combined with the OLR climatology to estimate a probability of convective influence. This scheme is described in Dessler *et al.* [2007] and SD11. The main disadvantage of this convective parameterization scheme is that it is climatological rather than year specific, and thus, the convective injection of ice and water may not be consistent with a specific year's tropical dynamics nor with specific observations. For this study we use Modern-Era Retrospective Analysis for Research and Applications (MERRA) anvil ice product (described below) to account for deep convective impact.

## 2. Model Description and Data Used

### 2.1. Trajectory Model

The isentropic trajectory model [Bowman and Carrie, 2002] follows the configuration described in SD11 and S12. Every 6 h 550 parcels are initiated on the 360 K isentrope over  $\pm 60^\circ$  latitude globally in a random pattern. If the net heating rate at 360 K is negative, the parcel is initialized just above the zero heating line at the same horizontal position. This insures that the parcel does not immediately begin to descend back into the lower troposphere.

At the end of each day, any parcels that have descended below the 355 K level are removed since we consider those parcels to have reentered the troposphere. The upper boundary is  $\sim 2200$  K isentrope ( $\sim 1$  hPa or  $\sim 50$  km), and parcels reaching the top are also removed. After a few years of integration, the system reaches quasi steady state with 250,000 parcels. Methane oxidation is included as described in SD11, but it has no impact on the analysis in this paper. We initiate the model in the year 2000, and we focus on analyzing the model results in 2008/2009 in order to compare the results to MLS, High Resolution Dynamics Limb Sounder (HIRDLS), and CALIOP observations. For this study we restrict ourselves to using the MERRA meteorological data set because of the availability of the anvil ice product [Rienecker *et al.*, 2011, and references therein].

### 2.2. The Cloud Model

Our CM is based on the simplified model described in FB06. The CM is a zero-dimensional model following the air parcel. The saturation level needed to initiate cloud formation is a CM input parameter (e.g., 100% relative humidity (RH)). When the saturation level is exceeded, the CM is initialized with a number of ice nuclei ( $N$ )

depending on the parcel cooling rate and temperature.  $N$  is estimated using the results from Kärcher *et al.* [2006]. We use the cooling rate from the meteorological analyses, which neglects short-period ( $<12$  h) temperature oscillations that might increase or decrease the MERRA-derived cooling rate. These high-frequency waves would likely increase cooling rates and thereby increase the concentration of small ice particles which settle slowly. As we show below, and as might be expected, short-period temperature oscillations are inefficient dehydrators, but small ice particles formed by short-period oscillations could affect cloud formation.

Total ice mass is computed from the ice volume mixing ratio and the density of ice at the temperature of the parcel. The ice particle effective radius ( $R$ ) is determined by dividing the ice mass among the  $N$  particles assuming they are spheres.  $N$  and  $R$  are dynamic, but only a single size mode is allowed. We save the ice and water vapor mixing ratios, as well as  $R$  and  $N$  at each CM time step.

Once ice particles are formed in the CM, we calculate deposition growth rates based on the local temperature, saturation level, and  $R$ . Ice deposition and particle growth deplete the vapor in excess of saturation. If ice is present and the parcel water vapor mixing ratio falls below saturation, ice particles begin to sublimate and subsequently decrease in size. Ice particles can also gravitationally sediment out of the parcel. We compute the ice sedimentation velocity assuming spheres using the Stokes drag expression [Locatelli and Hobbs, 1974]. In order to estimate ice loss, we must assume that the parcel has a “cloud thickness” as discussed below. Ice sedimentation reduces  $N$  so if vapor deposition on ice particles continues, it will occur on fewer and fewer ice particles resulting in more rapid particle growth followed by accelerated ice loss through sedimentation. Once the number of cloud particles falls below one particle per cubic meter, we set the vapor level to 100% relative humidity and the cloud is terminated.

Because the processes of vapor deposition, sublimation, and sedimentation can be very rapid, the CM operates independently of the trajectory model. For each parcel, the temperature and pressure are computed for each 6 h analysis period then the CM is run over the same period. The CM output is then interpolated back onto the coarser time grid of the trajectory model.

The simplified CM captures the essential role of TTL cloud formation in slowing dehydration of air; however, it does not account for a number of other cloud processes. These include carrying an actual particle size distribution (to more accurately compute ice sedimentation), aggregation of ice crystals, latent heating and cooling, and radiative heating effects on both temperature and small-scale dynamics. Including these effects is beyond the scope of this study, and it can be argued that they are second-order processes (FB06). The CM can include the effects of ice falling into the parcel from higher levels, but we have determined from off-line experiments that including this process has a very small effect on the final dehydration of the parcel because the final dehydration value is, to first order, controlled by temperature. Nonetheless, moistening lower layers would likely increase cloudiness at lower altitudes.

We have also experimented with setting the cloud initial saturation levels to  $>100\%$  RH since there is good laboratory and observational evidence that cloud formation not connected to convection occurs at supersaturation levels greater than 100% RH [Koop *et al.*, 2000; Jensen *et al.*, 2013]. Setting the supersaturation limit to a higher value produces more rapid initial ice particle growth compared to lower supersaturation levels because once ice particles form, there is relatively more rapid vapor deposition and more rapid particle growth. The more rapid ice particle growth increases parcel dehydration by about 3% because of increased gravitational sedimentation. However, as shown in SD11, if the saturation RH is increased, the stratospheric water vapor will increase because wetter parcels will on the average make it into the stratosphere without undergoing dehydration. For example, in a run where ID is used, if the saturation level is set to 120% RH, then stratospheric water vapor increases about 0.2 ppmv. Setting the ID threshold to 120% is, of course, different from setting the nucleation threshold to 120%, and this difference needs to be explored further. Higher-saturation levels for the onset of nucleation reduce the model cloud fraction mostly because fewer nucleation events occur. For the experiments shown in this paper, a condensation threshold of 100% RH is used, and the sensitivity to the nucleation threshold RH will be explored in future work.

Figure 1 shows the CM response to an oscillating temperature field in which the parcel experiences two saturation events in this example. When the cooling parcel first exceeds saturation, ice particles form, grow, and fall out and the parcel starts to dehydrate. When the parcel temperature begins to increase, ice begins to sublimate in order to maintain 100% RH. Finally, CM runs out of the ice available to hold the parcel at

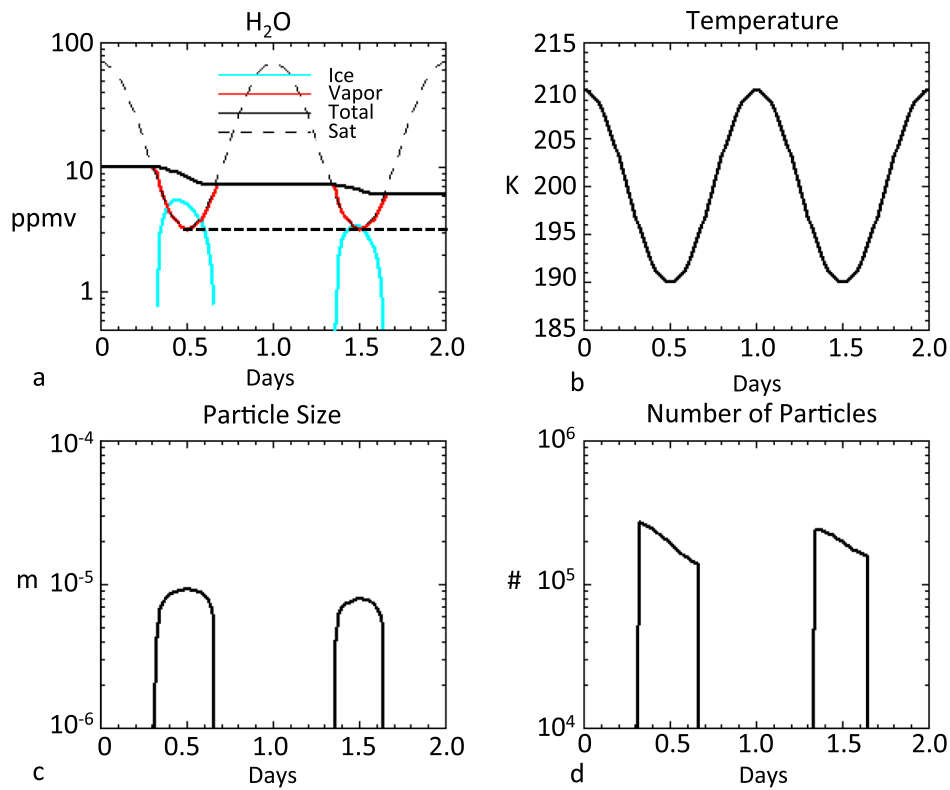


**Figure 1.** Cloud simulation at 100 hPa using our cloud model. (a) The total water content (ice plus vapor, solid line, black), the vapor amount (red) and the ice amount (blue), and the saturation mixing ratio (dashed) during the 2 day integration. (b) The initial water vapor amount is 10 ppmv, and parcel temperature varies. When saturation is triggered, a large number of particles are initiated based on the cooling rate and temperature. (c) The particle size grows and (d) ice begins to fall out of the volume which decreases the number of particles. Once the temperature becomes warmer (Figure 1b) than saturation, the ice begins to evaporate, size decreases (Figure 1c), and the ice mixing ratio falls (Figure 1a, blue line). The solid dashed curve in Figure 1a indicates the results if instantaneous dehydration (ID) is used. Cloud thickness is 500 m.

saturation, and the cloud terminates. The net effect of cloud formation is to slow the dehydration process relative to ID since it takes a finite time for ice particles to grow and fall out.

FB06 noted that efficiency of cloud dehydration is proportionally reduced as the temperature oscillation frequency is increased. This result is confirmed in Figure 2 which shows that the dehydration efficiency is defined as the ratio of ice lost to maximum amount of ice formed as a function of the wave period and cloud thickness. This result shows that short-period gravity waves are inefficient dehydrators because the timescale for cloud formation and ice sedimentation is approximately the same timescale as the short-period waves. Figure 2 also shows that dehydration efficiency varies with cloud thickness with deeper clouds are less efficient dehydrators because a smaller total fraction of the ice is removed from thicker clouds. The cloud thickness is an external parameter for the CM and thus is a source of uncertainty. In order to be more quantitative about our choice of cloud thickness, we turn to observations. Figure 3 shows January and July 2009 CALIOP tropical cloud thickness statistics for clouds with tops >14.5 km. The statistics reveal a clear peak in cloud thickness between 300 and 900 m with the mode at ~500–600 m. For our simulations, we assume a cloud thickness of 500 m to be consistent with observations.

### 2.3. Convective Moistening

Parcel moistening by convection or convective hydration is an input parameter to the model. There are several approaches to including convective hydration. As mentioned above, in SD2011 we have previously used a climatological parameterization of the altitude and location of convection [Dessler *et al.*, 2007]. This parameterization was a multiyear average, so it contained no information about year-to-year variability. An alternative approach is to separately compute the cloud altitude and location based on the observed OLR

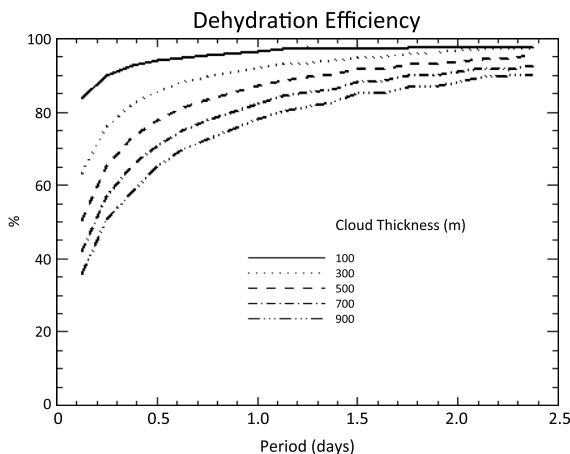


**Figure 2.** Cloud model dehydration efficiency versus thermal oscillation period for different thickness clouds. Cloud model was run for 10 days. Efficiency is defined as the percent of water lost compared to the amount that would be removed if the water vapor mixing ratio were adjusted to saturation at the minimum temperature. Short-period waves (few hours) are roughly half as efficient at removing water vapor as waves with periods longer than a day. Thicker clouds are less efficient at dehydrating because the fractional ice loss is less. Other than temperature frequency and cloud thickness, the model variables are the same as in the experiment shown in Figure 1.

We have created daily average anvil ice fields from the MERRA 3 h data. Once each day, the trajectory model locates parcels that intersect MERRA convective regions, and we linearly interpolate the MERRA anvil ice field onto those parcels.

Four basic experiments are described below and listed in Table 1. For the NC case, no convective influence is allowed. In the SC case, for parcels influenced by convection, the parcel water vapor concentration is reset to the local saturation mixing ratio. For the ASC case, the parcel water vapor is set to the saturation mixing ratio and convective ice is added. Finally, the ASC-wave case is the same as the ASC case, but wave-induced temperature perturbations are added to the MERRA temperature field.

Figure 4 shows the December-January-February (DJF) 2008/2009 and June-July-August (JJA) 2008 time mean MERRA anvil ice concentration maps averaged between 14 and 18 km along with the zonal means. In DJF, the largest anvil ice concentration is in the Southern Hemisphere and concentrated over Northern Australia extending along the southern branch of the Intertropical Convergence Zone. Anvil ice does not extend much above 370 K. In JJA, there is significantly more anvil ice and it is concentrated in the Northern Hemisphere spreading from India toward the tropical West Pacific. A second enhanced anvil region is located over Mesoamerica. The summer anvil ice has about the same vertical extent as winter anvil ice but is much closer to the tropopause. This means that there is a higher probability of convective moistening above the tropopause in summer than in winter.

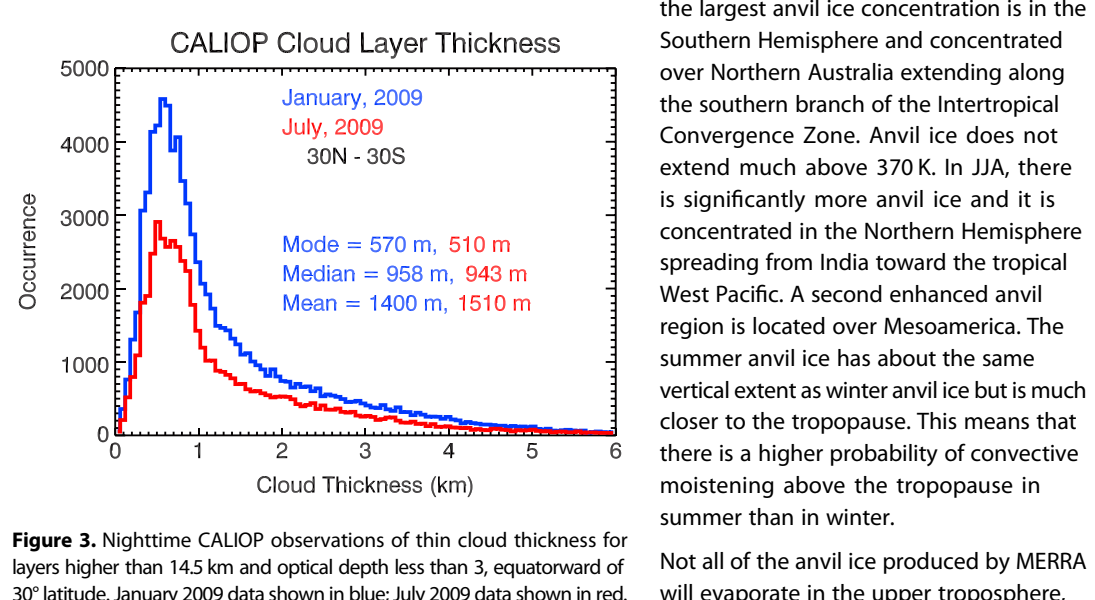


**Figure 3.** Nighttime CALIOP observations of thin cloud thickness for layers higher than 14.5 km and optical depth less than 3, equatorward of 30° latitude. January 2009 data shown in blue; July 2009 data shown in red.

and/or CloudSat observations and then to compare the results with the trajectory positions at specific observational times. This would provide more precise information on convective hydration. Unfortunately, the convective fields thus generated would be inconsistent with the assimilated MERRA wind and temperature fields. Therefore, for simplicity, we will use MERRA fields in this study despite the issues with MERRA convection described below.

MERRA generates convective clouds using a relaxed Arakawa-Schubert (RAS) scheme [Moorthi and Suarez, 1992] that estimates convective mass fluxes as a sequence of idealized convective plumes. The adaptation of RAS to GEOS-5 (the core of MERRA) is described in Waliser *et al.* [2009]. MERRA outputs two relevant cloud ice products: stratiform or large-scale ice and convectively produced anvil ice. We are interested in the anvil ice because the trajectory model already simulates stratiform clouds.

Not all of the anvil ice produced by MERRA will evaporate in the upper troposphere,

**Table 1.** Trajectory Model Cases

Case	Description
NC	No convective influence
SC	Parcels set to saturation in convection zones
ASC	Anvil ice added and parcels set to saturation in convection zones
ASC-wave	Same as ASC but wave-modified MERRA temperatures

because MERRA anvil ice effective radius is large,  $\sim 70 \mu\text{m}$  (L. Oman, personal communication, 2014) and most of this ice would fall out of the TTL without evaporating. Nonetheless, some fraction of the ice generated by MERRA will fall more slowly and may enhance the total water concentration. Until recently, particle probes have

reported a large number of small ice crystals ( $< 10 \mu\text{m}$ ) in anvil cirrus and that the particle size decreased with radius following an approximate  $-2.5$  to  $-3$  power law [e.g., Knollenberg *et al.*, 1993]. More recent measurements using open-path particle probes have suggested a much smaller number of small crystals implying that the previous high numbers were due to shattering artifacts on probe inlets [McFarquhar *et al.*, 2007; Jensen *et al.*, 2009]. If we assume a size distribution roughly equivalent to that reported during TC-4 from 2D-S probes, the effective radius is  $30$ – $60 \mu\text{m}$ . Roughly integrating the ice mass over the observed size distributions reported by the 2D-S, we find that ice mass fraction smaller than the  $30 \mu\text{m}$  is roughly 1–2% of the total ice mass—ice particles larger than that will fall out too quickly to be available for additional hydration. The disparity between the MERRA effective radius and observations motivates the two limiting cases that we consider: ASC, which adds anvil ice from MERRA to the parcels, and SC, in which parcels are set to saturation, implying that the convective ice particles are too large to effectively increase the parcel total water.

MERRA data products do not report the ice particle equivalent radius. Thus, when ice from MERRA is added, we form a new cloud if one does not exist. The ice particle size is determined by the cloud initiation algorithm described section 2.2. If the cloud already exists, then the existing cloud particle number is conserved and the particle radius is increased to account for the added ice volume. This approach is going to overestimate the influence of convective ice, because as noted above, only a small fraction of the convective ice will have

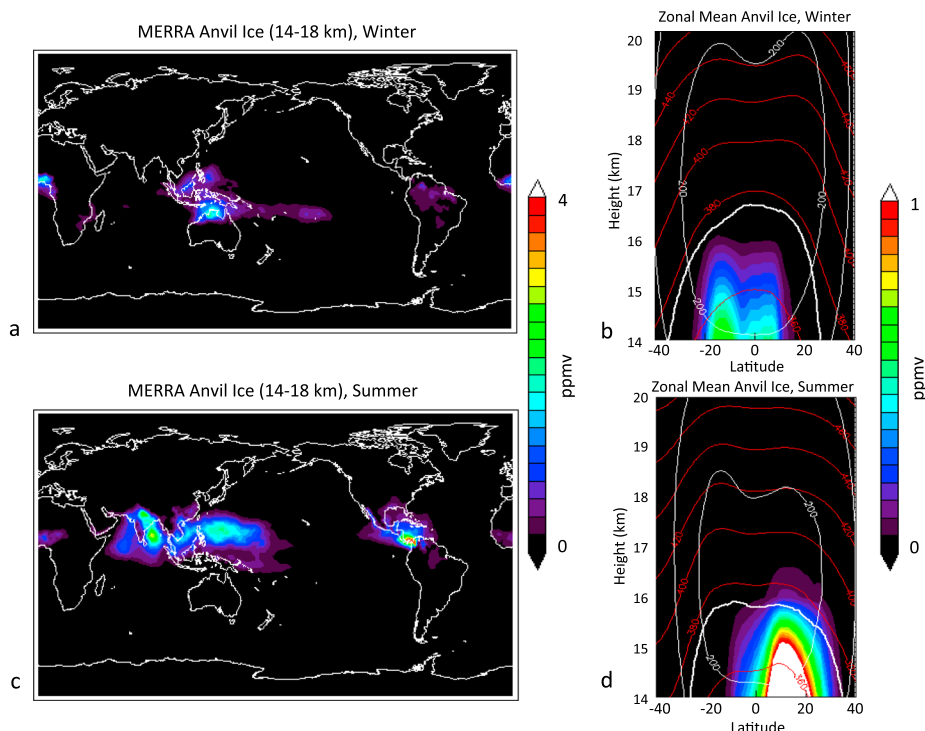


**Figure 4.** MERRA anvil ice for (a and b) winter (DJF 2008/2009) and (c and d) summer (JJA 2009). Maps of averaged anvil ice between 14 and 18 km in ppmv are shown in Figures 4a and 4c (scale 0–4 ppmv). Zonal mean values are shown in Figures 4b and 4d (scale 0–1 ppmv). Thick white line is the zonal mean tropopause; red lines are potential temperature contours spaced every 20 K; the line just above the tropopause in each figure is 380 K.

**Table 2.** Global Average Stratospheric Water Vapor, DJF 2008/2009, 18–30 km<sup>a</sup>

MLS: 4.57	Cloud Dehydration	Instant Dehydration
ASC-wave	4.73	3.42
ASC	4.92	3.73
SC	4.59	3.73
NC	4.33	3.83

<sup>a</sup>Units are in ppmv.

radii small enough not to settle out almost immediately. In effect, this assumption upper bounds the role of convective ice.

#### 2.4. MERRA Temperatures and Wave Modification of MERRA Temperatures

Because upper troposphere temperature provides the main control of stratospheric water vapor,

we have compared MERRA temperature fields to global positioning satellite radio occultation (GPS-RO)-derived temperatures [Anthes *et al.*, 2008; Ho *et al.*, 2009] to understand what biases might exist. The detailed comparison is documented in Wang *et al.* [2014b]. MERRA has a warm bias at the tropical tropopause of 0.1–0.4 K that would produce a 0.08–0.4 ppmv moist bias in entry level of stratospheric water vapor assuming 100% saturation. This warm bias is most apparent outside the tropical West Pacific; however, SD11 shows that most of the air entering the stratosphere has its final dehydration in the tropical West Pacific where the bias is small. The net result of running our trajectory model using GPS-RO temperatures instead of MERRA temperatures is to produce a < 2.5% (< 0.1 ppmv) decrease in stratospheric water vapor relative to running the model with MERRA temperatures [Wang *et al.*, 2014b].

Wave-generated temperature disturbances near the tropical tropopause can be underrepresented due to the relatively coarse MERRA vertical resolution at that altitude (1.5–2 km). In order to overcome this bias, a new wave enhancement scheme was introduced by Kim and Alexander [2013]. For each grid point in MERRA temperature, a Fourier transform is applied to a 90 day time series to get wave amplitudes and phases. The wave amplitudes are then amplified or attenuated to match the variance indicated by nearby radiosondes. The amplitude and phase profiles in Fourier space are then interpolated separately onto finer 200 m vertical levels near the tropopause to recover the temperature variability induced by waves. This scheme does not add higher-frequency waves but increases the amplitude of existing waves and correctly interpolates those wave temperatures onto the region between MERRA levels. As noted above, adding temperature fluctuations from higher-frequency waves is probably less important than correctly enhancing and interpolating the existing wave temperatures because the higher-frequency waves are inefficient dehydrators (Figure 2). Applying this wave scheme to MERRA temperature records yields an adjusted MERRA temperature data set that has a slightly cooler tropopause minimum field compared to MERRA [Wang *et al.*, 2014b]. The cooler tropopause reduces the stratospheric water vapor as shown in Table 2 below.

#### 2.5. Satellite Observations of Cirrus

Massie *et al.* [2013] compared tropical high cloud frequency observations from five different satellite data sets: Stratospheric Aerosol and Gas Experiment II, Halogen Occultation Experiment, Cryogenic Limb Array Etalon Spectrometer, HIRDLS, and Cloud-Aerosol Lidar with Orthogonal Polarization (CALIOP). They found good agreement among the various data sets even though the techniques were quite different. The cloud climatology reported by Massie *et al.* is also consistent with OSIRIS [Bourassa *et al.*, 2005] and ICESat [Dessler *et al.*, 2006] observations.

Avery *et al.* [2012] looked at CALIOP, MLS, and CloudSat cloud ice retrievals and concluded that MLS and CloudSat underreported small ice crystals relative to CALIOP, and MLS ice water content retrievals are quite noisy at high altitudes [also see Wu *et al.*, 2013]. HIRDLS and CALIOP data are the most relevant observational data sets for this study since they have better vertical coverage and are sensitive to small particles. We have independently compared HIRDLS and CALIOP 2008 cloud frequency data, and they show quite good agreement. We will focus solely on CALIOP measurements for our model comparisons because of CALIOP's higher sensitivity.

The CALIOP backscatter lidar on the CALIPSO satellite began making measurements in June of 2006 and observes at 532 and 1064 nm lidar backscatter [Winker *et al.*, 2010], with a perpendicular channel at 532 nm providing measurements of depolarization. The cloud and aerosol layer detection algorithms are discussed in Vaughan *et al.* [2009] and subsequent extinction retrievals in Young and Vaughan [2009]. The CALIOP

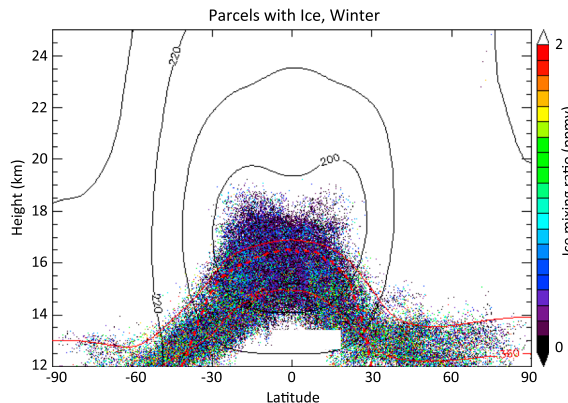


**Figure 5.** The ensemble of all ice-containing parcels for nine output days DJF 2008/2009. Colors indicate ice mixing ratio in ppmv. This is a subset of the  $\sim 3 \times 10^6$  parcels in the total DJF 2008/2009. Zonal average MERRA temperatures (K) are shown in black. Red lines indicate the 360 K (lower line) and 380 K (upper line) potential temperature surfaces and the tropopause (dashed red line).

Version 3 algorithms use the magnitude and variability of lidar backscatter at 532 and 1064 nm as well as the 532 nm volume depolarization and 1064/532 backscatter ratio to discriminate between clouds and aerosols [Liu *et al.*, 2009] and between liquid and condensed water [Hu *et al.*, 2009]. The CALIOP nighttime measurements have higher S/N than daytime measurements, so we restrict our analysis to nighttime data. We screen the V3 CALIOP 5 km profile data for clouds with  $> 0.01 \text{ mg/m}^3$  of ice, which corresponds to an extinction threshold of  $\sim 1.6 \times 10^{-3} \text{ km}^{-1}$ . This threshold is low enough for thin cloud detection but high enough to suppress most false positive cloud identification at night. We use the same ice threshold in the analysis of the model results.

### 3. Trajectory Modeling Results

The four basic trajectory model runs are described above and outlined in Table 1. In addition to each of these runs, we perform the same computation using instantaneous dehydration (ID) instead of CM dehydration. The instantaneous dehydration cases are labeled “ID” in Table 2. These four basic computations allow us to assess the role of convective moistening and cloud processing in the determining stratospheric water vapor. For reference, the SD11 water vapor calculations are closest to SC-ID case.

#### 3.1. Boreal Winter 2008/2009

In Figure 5 we show the distribution of ice-containing parcels for the DJF 2008/2009 period, ASC case. Subsequent figures will show this parcel data averaged and gridded. Figure 5 shows that all ice-containing parcels are present above the zonal mean tropopause both in the tropics and in the extratropics because of synoptic and mesoscale variations in local tropopause height. Ice mixing ratios tend to be lower in the upper troposphere due to the colder temperatures and lower water vapor amounts—a result of previous dehydration events. Because parcels are initiated near 360 K, there are few parcels containing ice below  $\sim 360 \text{ K}$  in the model tropics.

##### 3.1.1. Zonal Mean Cloud Comparison

Figure 6 shows a comparison between CALIOP cloud frequency, MERRA total cloud fraction (anvil + large scale), and the trajectory model cloud fraction with anvil ice added (ASC), saturation over convection (SC), and without convection (NC). Because we are including convection in the ASC and SC runs, we are effectively modeling both convective and in situ generated stratiform clouds. The NC case would only simulate in situ formed clouds. Thus, we expect that many fewer clouds will be present in the NC case as will be seen below.

Comparing NC with SC and ASC, we see that convection increases the cloud fraction in the TTL by a factor of 2–3 and brings the model cloud fraction into reasonable agreement with CALIOP observations. MERRA cloud fraction more closely resembles the NC case above 15 km, which is not surprising given that the equivalent radius of MERRA ice is so large that most of the cloud ice has fallen out. Both the model and MERRA cloud fraction show a wider meridional tropical cloud extent compared to CALIOP observations. They also show a minimum in the cloud distribution at the equator, a minimum not evident in the CALIOP data. This minimum partially arises from a corresponding minimum in convection evident in MERRA (Figure 3b), but even without convective input (NC), an equatorial minimum still is present due to relatively warmer temperatures at the equator compared to the adjacent regions.

A more quantitative cloud fraction comparison among the three cases to CALIOP is shown in Figure 7. The SC case agrees reasonably with CALIOP observations below 16 km ( $\sim 100 \text{ hPa}$ ), NC is too low by a factor of  $\sim 2$ , and ASC is 30% too large. We limit the model convective ice input to potential temperatures below 380 K since observations rarely show clouds above that level [Liu and Zipser, 2005]. Nonetheless, the model does

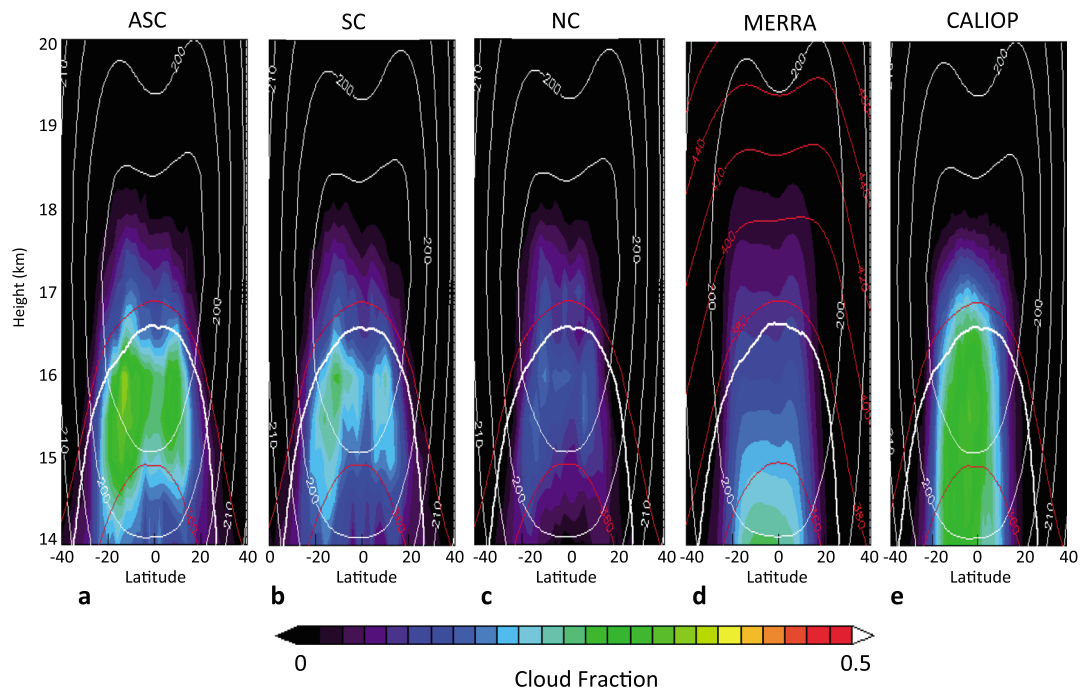


**Figure 6.** Zonal mean DJF 2008/2009 cloud fraction from trajectory simulation including (a) anvil ice (ASC) and (b) without anvil ice but air is saturated by convection (SC) in both cases, (c) no convective influence (NC), (d) MERRA cloud fraction, and (e) CALIPSO cloud frequency for same period. Zonal mean temperatures are white thin contours, potential temperature surfaces are red lines (20 K spacing, 380 K surface is just above the tropopause, and tropopause is thick white line).

simulate the decrease in cloud fraction with height as observed by CALIOP. Between 15 and 16 km, the NC cloud fraction is about 55–60% of observed. This means that about 40–45% of clouds are due to convection. The ASC simulation creates 30% more clouds compared to CALIOP suggesting the injection of all of the MERRA ice is not needed to explain the cloud fraction due to convection. Wang and Dessler [2012] using CALIOP and MLS data obtained a lower limit of 30% for convectively generated cirrus, and Riijimaki and McFarlane [2010] estimated a lower limit of 36%. Our 40–45% number suggests that this limit is even

higher. The difference between our estimate and the lower estimates arises because those studies only considered the local contribution of convective clouds in forming cirrus. Our model includes the possibility of convectively generated cirrus, subsequently evaporating and then reforming elsewhere—disconnected from the local convection zone as observed by Pfister *et al.* [2001].

### 3.1.2. Water Vapor

Figure 8 shows the zonal mean water vapor fields for ASC, SC, NC, and SC-ID. In SC-ID case we set the parcels encountering convection to saturation, but subsequently, we use ID. The driest stratospheric field is SC-ID and the wettest ASC. The cases show roughly constant offsets between each other except in the tropical tape recorder. Global average water vapor fields between 18 and 30 km and MLS averages are shown in Table 2. Stratospheric water vapor is on the average ~1 ppmv higher when the CM is

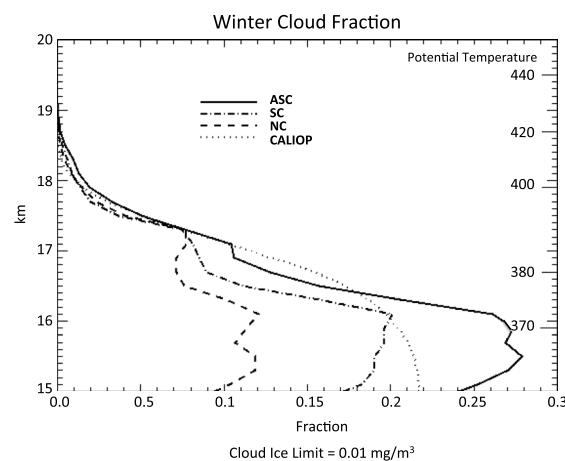


**Figure 7.** Comparison of cloud fraction from model with and without convective clouds. The cloud fraction shown is an average over the tropics ( $\pm 20^\circ$ ) and is compared to CALIOP tropical observations for DJF 2008/2009. Approximate potential temperature is shown at right. See Table 1 for cases.

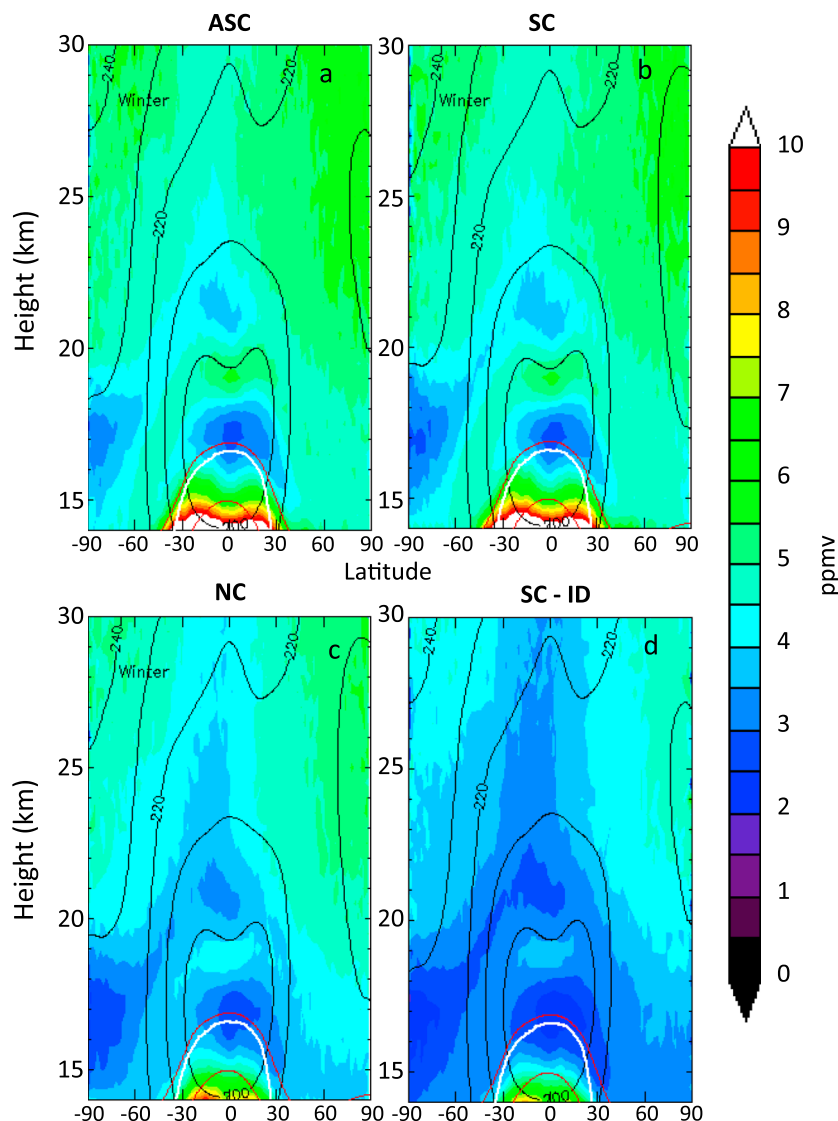


**Figure 8.** Zonal mean water vapor plots for boreal winter 2008/2009. (a) Cloud dehydration plus anvil ice (ASC), (b) saturation but no added ice (SP), (c) cloud dehydration and no convection (NC), and (d) ASC with ID. Red lines are as in Figure 4; tropopause is thick white line.

used instead of ID for the ASC and SC cases. Even with no convection, ID produces a stratosphere that is about 0.5 ppmv drier than with cloud dehydration.

We conclude that the use of the CM adds 0.5 ppmv and that convection adds about 0.6–0.5 ppmv more (ASC minus NC = 0.6 ppmv, SC minus NC = 0.5 ppmv). The use of wave-modified MERRA temperatures lowers the water vapor by 0.2 ppmv.

The ASC (same as Figure 8a) and MLS zonal mean DJF 2008/2009 water vapor fields are shown in Figures 9a and 9b. Figure 9c shows the equatorial profiles for the four cases described above (ASC, SC, NC, and SC-ID). The MLS minimum in tropical water vapor at 23 km is about 1–2 km higher than any of the model cases. This is likely due to the slower tropical ascent rate in MERRA compared to observations as shown in S12.

Figure 9c shows that the tropical water vapor amounts for the different cases are seasonally dependent. Above the tropopause (~18 km) there is a significant increase in stratospheric water when convection is included. At 19 km, representing the input of water in the boreal summer, the difference between the MLS observations and the ASC case is almost 2 ppmv. This is likely due to the much larger convective influence and subsequent injection of ice in the summer (see Figure 3d) [Lelieveld et al., 2007; Randel and Jensen, 2013].

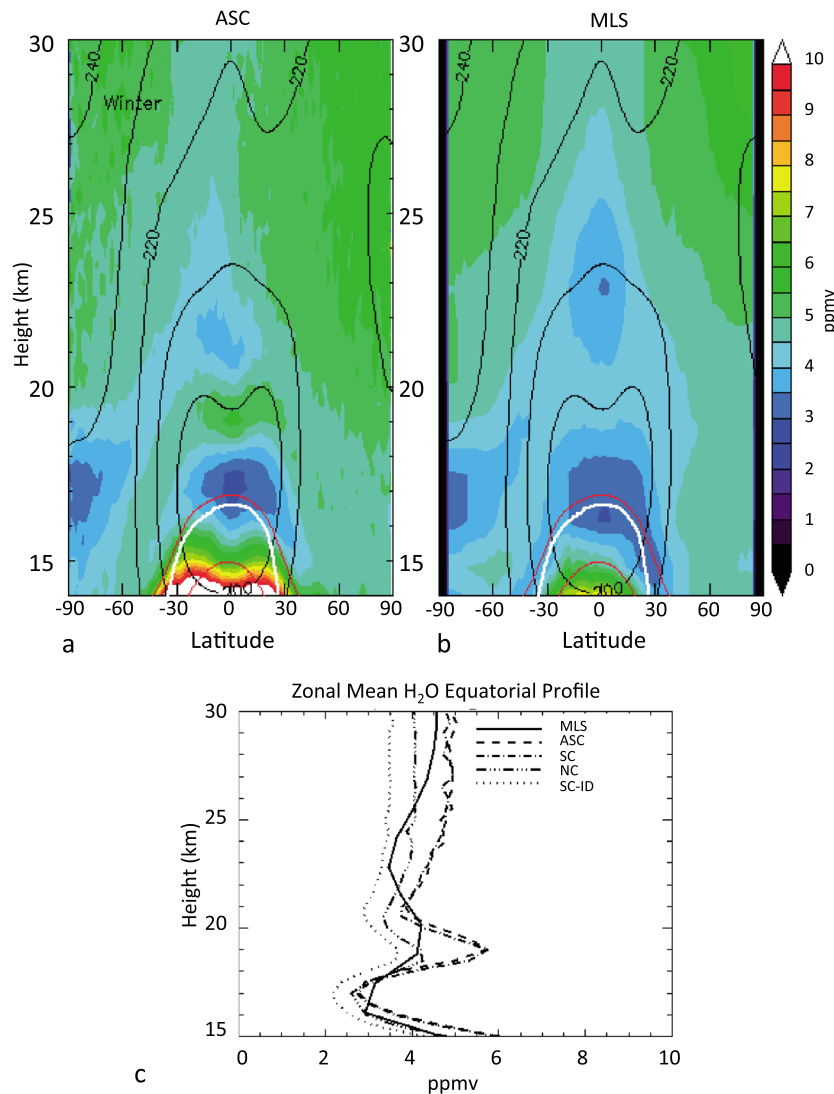


**Figure 9.** (a) Zonal mean DJF 2008/2009 model water vapor as in Figure 7a (ASC). (b) MLS observations over the same period. (c) Equatorial water vapor profiles from the model experiments. See Table 1 for cases.

Consistent with Figure 9, Table 2 shows that including ice injection (ASC) increases the average stratospheric water vapor over observations by only 10% suggesting that actual ice input is not as important as the saturating air in the presence of convection. The impact on clouds is much greater as shown in Figure 7 where the cloud frequency increase between SC and ASC is closer to 35%. The SC case is quite close to the observed MLS water vapor amounts and the CALIOP cloud frequency.

### 3.1.3. Cloud Distributions

Boreal winter cloud fraction maps for DJF 2008/2009 compared to CALIOP are shown in Figure 10. These maps show the vertically integrated cloud fraction from 15 to 18 km. Figure 10a shows that the CALIOP high clouds are confined to three distinct regions: western Pacific/maritime continent, South America, and Africa with relatively cloud-free regions in between. This is consistent with HIRDLS, OSIRIS, and ICESat measurements. The cloud fraction over the West Pacific maritime continent is the greatest, rising to 20%.

The model cloud fraction (Figures 10b and 10c) for the ASC and SC cases agrees quite well with observations (Figures 10b and 10c). In general, both the ASC and SC simulations show more clouds compared to observations over Africa and South America. Figure 7 shows that ASC has overall ~30% more clouds than SC below 16 km. This is evident in the cloud maps with relatively more clouds in ASC than SC. The simulations show a distinctive minimum in cloud fraction at the equator also evident in Figure 6. In S12 we noted that

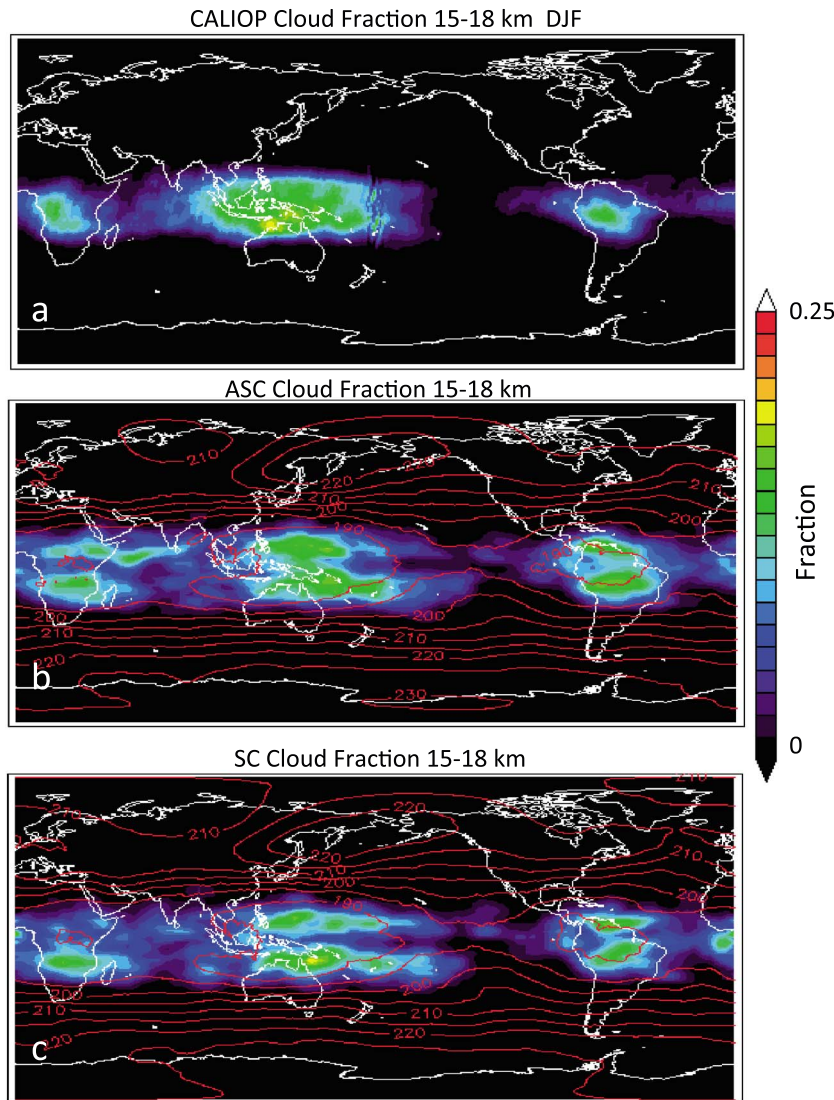


**Figure 10.** Cloud fraction 15–18 km averaged over DJF 2008/2009. (a) From CALIPSO, (b) ASC, and (c) SC. Red contours show the 17 km temperature from MERRA.

the final dehydration pattern in MERRA showed a similar bifurcation. Bifurcation of the dehydration pattern is also evident in the other reanalyses we have looked at (e.g., the ERA Interim Reanalysis), but the Southern Hemisphere maximum appears most pronounced in MERRA (S12, Figure 3).

### 3.2. Boreal Summer 2009

Figure 11 shows the model zonal mean cloud fraction for JJA 2008 in the same format as the winter case (Figure 6). The cloud fraction with convection is similar to the CALIOP data although the model maximum is slightly north of the CALIOP maximum, and there is also a distinct Southern Hemisphere lobe of clouds not evident in the CALIOP data. The MERRA cloud fraction does not extend as high as CALIOP, but it is in better agreement with observations than the winter case. The ASC case produces about 30% too many clouds compared with CALIOP observations at 15 km and above, but SC case is in good agreement with CALIOP. This result is similar to the boreal winter case. Without the convection, the cloud fraction is too low compared to CALIOP as was also seen in the winter case (Figure 6c).

Figure 12 shows the zonal mean JJA 2009 water vapor as in Figure 8. As was seen in the boreal case, CM dehydration along with convection produces an increased stratospheric water vapor field compared to the NC case (Figure 12c) and SC-ID case (Figure 12d). Also evident in these figures is the strong

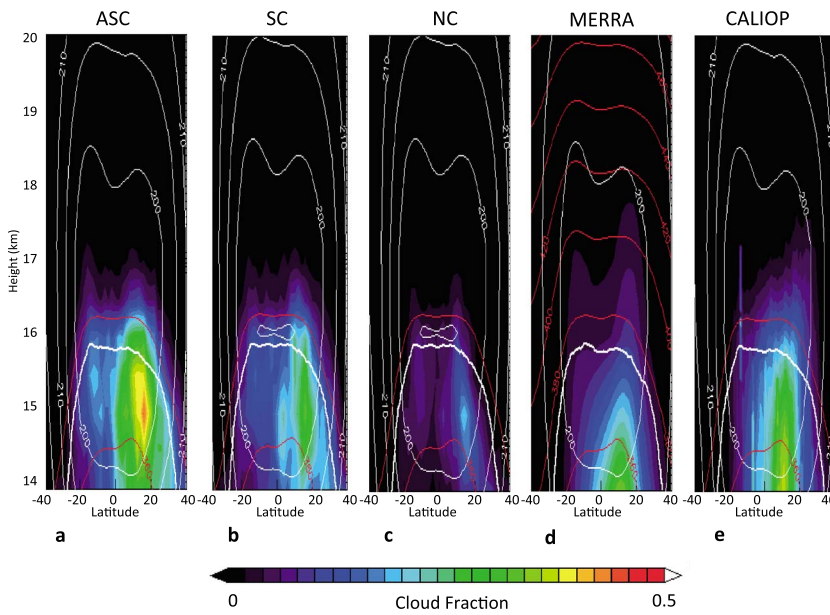


**Figure 11.** Same as Figure 6 except for JJA 2009.

dehydration over Antarctica. The amount of Antarctic stratospheric dehydration is slightly reduced when cloud dehydration is used compared to ID.

Figure 13 shows the 15–18 km cloud fraction maps for JJA 2009 compared to the CALIOP cloud observations. Because the boreal summer cloud fields have lower altitude than in winter, the cloud fraction above 15 km is significantly smaller. Overall, the ASC and SC simulations put clouds too far east of observations, and simulations fail to form a distinct cloud field east of the Himalayan Plateau. When convective ice is included, the model produces too many clouds over the West Pacific and over Mesoamerica compared to CALIOP, which shows the highest cloud fraction over the Himalayan Plateau. The MERRA anvil ice distribution along with our model results suggests that MERRA is underestimating the convection in the monsoon region and generating too much convection in the tropical West Pacific.

Tracer analysis [Randel *et al.*, 2006, 2010; Wang *et al.*, 2014a] suggests that there is significant transport of CO and other gases up through the Asian Monsoon region through deep convection. The model simulations suggest that MERRA convective systems are shifted too far east as seen in Figure 4, and this is a consistent feature. These GEOS-5/MERRA convection issues are also noted in Wu *et al.* [2009] and Jiang *et al.* [2010].

#### 4. Summary and Discussion

A Lagrangian cloud model (CM) based on Fueglistaler and Baker [2006] is introduced to improve the realism of the dehydration process in our forward domain-filling trajectory model. Our previous calculations used “instantaneous dehydration” (ID) where the parcel water vapor mixing ratio is constantly adjusted to not exceed the saturation mixing ratio. In this paper we describe integrations using the trajectory CM. The CM converts water vapor above saturation to ice and computes the ice particle number density and size. As ice falls out of the cloud, total parcel water (vapor plus ice) is reduced but much more slowly compared to ID. The simulations described in this paper also use convective moisture input from the MERRA instead of our previous OLR-based convective moistening scheme (SD11).

##### 4.1. Cloud Dehydration Versus Instant Dehydration

The net effect of CM dehydration versus ID is to increase the lower stratospheric average water vapor by ~1 ppmv (Table 2, ~22% of the observed amount). We conclude that models that use ID will significantly underestimate the transport of water across the tropical tropopause and excessively dehydrate the stratosphere.

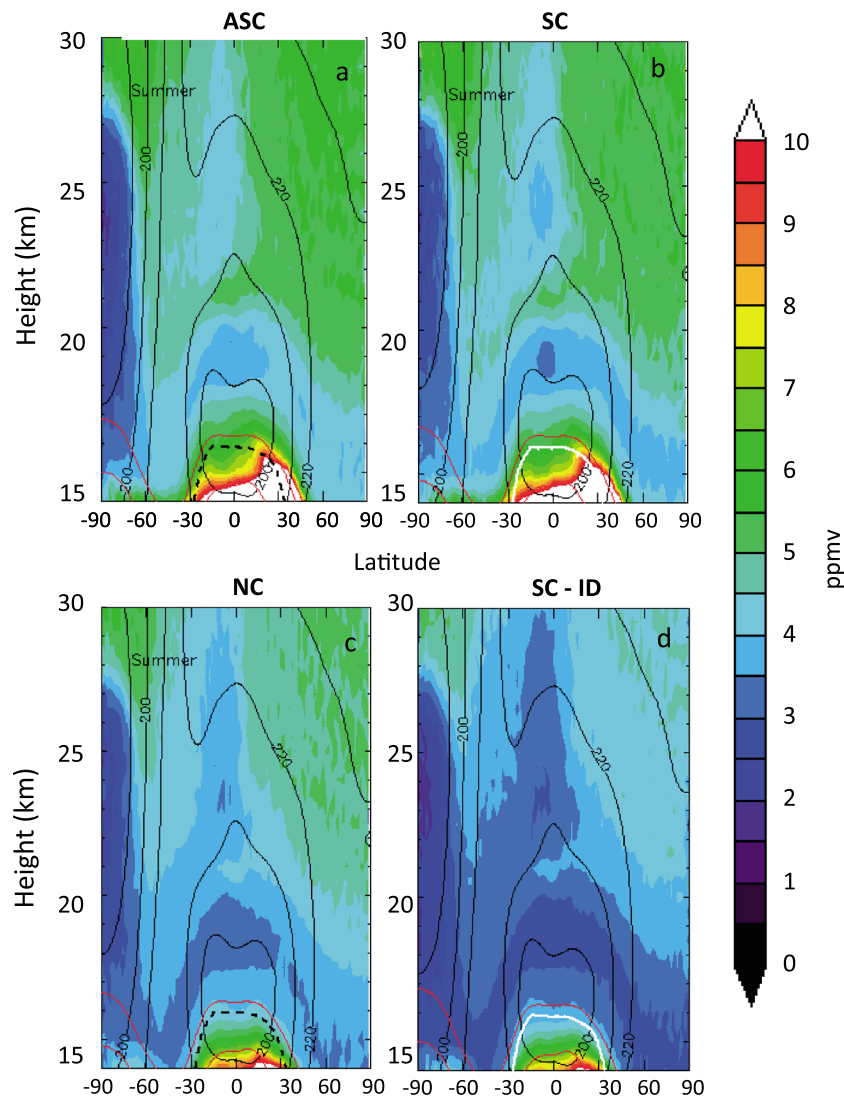


**Figure 12.** Same as Figure 8 but for JJA 2009.

#### 4.2. Convective Moistening

The net effect of convective moistening is to increase lower stratospheric water vapor up to ~13%. With convective moistening and cloud dehydration, the computed lower stratospheric water amount is very close to MLS observations (SC case). If we add convective ice, we increase stratospheric water by 0.33 ppmv. If we include wave modification of the MERRA temperature fields, the stratospheric water vapor drops by 0.2 ppmv.

#### 4.3. Cloud Fraction

Without convection, the model produces a significant deficit in TTL clouds compared to CALIOP observations. With convection, TTL cloud fraction increases by a factor of 2–3 depending on whether or not we inject ice along with convective saturation of the trajectory parcels. When ice injection is not included, our TTL cloud fraction is in rough agreement with CALIOP observations. Our model results suggest that convection is ultimately responsible for ~41% of the clouds in the TTL. This means that convection not only is responsible for anvil cirrus but also increases other types of cirrus. This attribution to convection is higher than the ~30–36% lower limit from previous estimates [e.g., Wang and Dessler, 2012; Riihimaki and McFarlane, 2010]. The reason for the higher value is that excess water vapor injected by the convective process can produce cirrus elsewhere—cirrus not obviously connected to active convection.

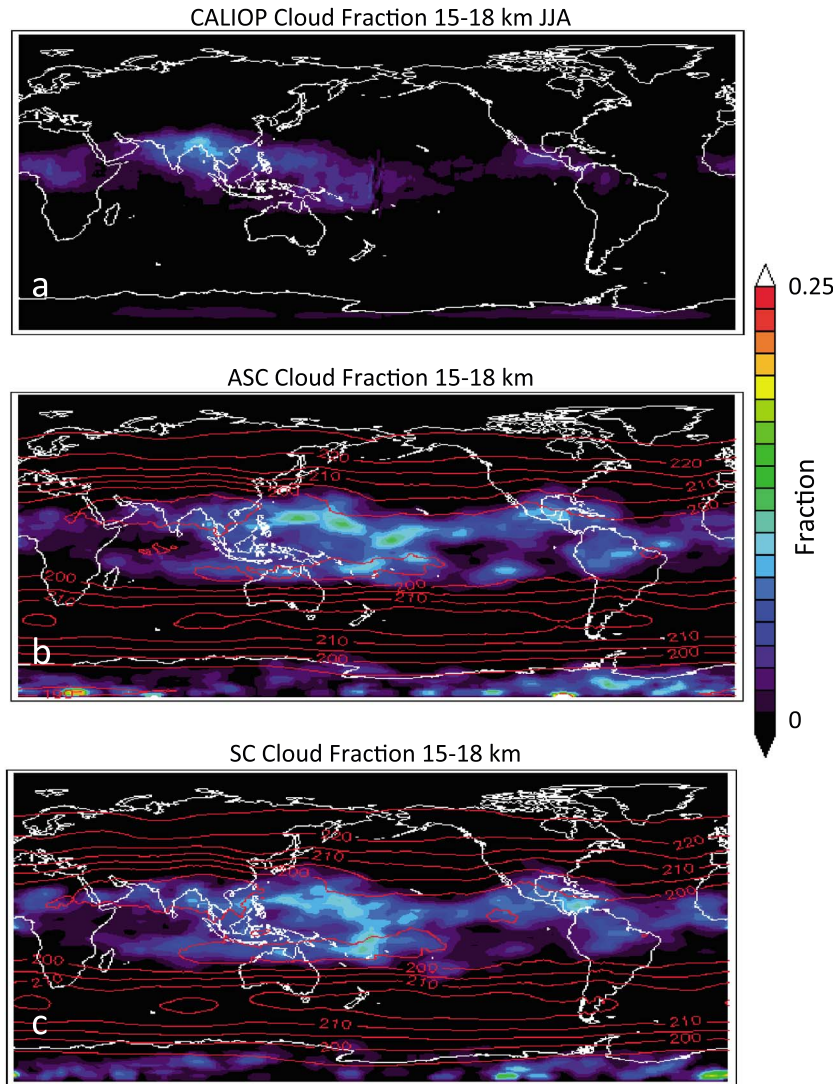


**Figure 13.** Same as Figure 10 but for JJA 2009.

Cloud fraction maps show broad agreement with CALIOP observations, but there are notable differences. In winter, we produce too many clouds in the Southern Hemisphere and over Africa and South America compared to CALIOP. During summer, the model does not produce the cirrus deck associated with the East Asian monsoon. Instead, the model clouds are displaced to the east. These differences are likely associated with biases in the location of MERRA convection and biases in the MERRA temperature fields.

#### 4.4. Implications of These Results

Our model results suggest a more significant role for convection in TTL cirrus production than previous studies. The most recent Intergovernmental Panel on Climate Change report [*Intergovernmental Panel on Climate Change (IPCC)*, 2013] as well as the previous report has identified tropical cirrus as a key element of the climate system. An increase in tropical cirrus will increase tropospheric warming [*Rondanelli and Lindzen*, 2010] as well as increase stratospheric water vapor [*Forster and Shine*, 1999; *Solomon et al.*, 2010]. In a future world where sea surface temperatures are warmer, convective injection of ice into the TTL and lower stratosphere will likely increase. Our results suggest that the increase in convection will increase the stratospheric water vapor and tropical cirrus even if the tropopause does not warm. The *IPCC* [2013] notes that there is “significant feedback uncertainty” in these mechanisms based upon model spread [*IPCC*, 2013, section 7.2.5.2, Figure 7.10]. The CALIOP measurements of cirrus and MLS measurements of water vapor provide important validation and constraints on TTL model simulations.

## Acknowledgments

We would like to thank Steve Massie for providing the HIRDLS cloud frequency data, Stephan Fueglistaler for the cloud model code from which the cloud model described here was developed, and the reviewers for helpful and insightful comments. M. Avery acknowledges funding from the CALIPSO project. CALIOP, MLS, HIRDLS, and MERRA data are available from NASA at no charge. This work was supported under NASA grants NNX13AK25G and NNX14AF15G and under the NASA Airborne Tropical Tropopause EXperiment (ATTREX).

## References

- Anthes, R. A., et al. (2008), The COSMIC/FORMOSAT-3 mission: Early results, *Bull. Am. Meteorol. Soc.*, **89**, 313–333, doi:10.1175/BAMS-89-3-313.
- Avery, M., D. Winker, A. Heymsfield, M. Vaughan, S. Young, Y. Hu, and C. Trepte (2012), Cloud ice water content retrieved from the CALIOP space-based lidar, *Geophys. Res. Lett.*, **39**, L05808, doi:10.1029/2011GL050545.
- Bouassa, A. E., D. A. Degenstein, and E. J. Llewellyn (2005), Climatology of the subvisual cirrus clouds as seen by OSIRIS on Odin, *Adv. Space Res.*, **36**, 807–812.
- Bowman, K. P., and G. D. Carrie (2002), The mean-meridional transport circulation of the troposphere in an idealized GCM, *J. Atmos. Sci.*, **59**, 1502–1514.
- Corti, T., et al. (2008), Unprecedented evidence for deep convection hydrating the tropical stratosphere, *Geophys. Res. Lett.*, **35**, L10810, doi:10.1029/2008GL033641.
- Dessler, A. E. (1998), A reexamination of the “stratospheric fountain” hypothesis, *Geophys. Res. Lett.*, **25**, 4165–4168, doi:10.1029/1998GL900120.
- Dessler, A. E., and S. C. Sherwood (2003), A model of HDO in the tropical tropopause layer, *Atmos. Chem. Phys.*, **3**, 2173–2181.
- Dessler, A. E., S. P. Palm, W. D. Hart, and J. D. Spinharne (2006), Tropopause-level thin cirrus coverage revealed by ICESat/Geoscience Laser Altimeter System, *J. Geophys. Res.*, **111**, D08203, doi:10.1029/2005JD006586.
- Dessler, A. E., T. F. Hanisco, and S. A. Fueglistaler (2007), Effects of convective ice lofting on H<sub>2</sub>O and HDO in the tropical tropopause layer, *J. Geophys. Res.*, **112**, D18309, doi:10.1029/2007JD008609.
- Forster, P. M. D., and K. P. Shine (1999), Stratospheric water vapour changes as a possible contributor to observed stratospheric cooling, *Geophys. Res. Lett.*, **26**, 3309–3312, doi:10.1029/1999GL010487.
- Fueglistaler, S., and M. B. Baker (2006), A modelling study of the impact of cirrus clouds on the moisture budget of the upper troposphere, *Atmos. Chem. Phys.*, **6**, 1425–1434.
- Fueglistaler, S., M. Bonazzola, P. H. Haynes, and T. Peter (2005), Stratospheric water vapor predicted from the Lagrangian temperature history of air entering the stratosphere in the tropics, *J. Geophys. Res.*, **110**, D08107, doi:10.1029/2004JD005516.
- Fueglistaler, S., A. E. Dessler, T. J. Dunkerton, I. Folkins, Q. Fu, and P. W. Mote (2009), The tropical tropopause layer, *Rev. Geophys.*, **47**, RG1004, doi:10.1029/2008RG000267.
- Ho, S.-P., et al. (2009), Estimating the uncertainty of using GPS radio occultation data for climate monitoring: Intercomparison of CHAMP refractivity climate records from 2002 to 2006 from different data centers, *J. Geophys. Res.*, **114**, D23107, doi:10.1029/2009JD011969.
- Hu, Y., et al. (2009), CALIPSO/CALIOP cloud phase discrimination algorithm, *J. Atmos. Oceanic Technol.*, **26**, 2293–2309, doi:10.1175/2009JTECHA1280.1.
- Intergovernmental Panel on Climate Change (IPCC) (2013), *Climate Change 2013: The Physical Science Basis, Contribution of Working Group I to the Fifth Assessment Report of the Intergovernmental Panel on Climate Change*, edited by T. F. Stocker et al., 1535 pp., Cambridge Univ. Press, Cambridge, U. K., and New York.
- Jensen, E., and L. Pfister (2004), Transport and freeze-drying in the tropical tropopause layer, *J. Geophys. Res.*, **109**, D02207, doi:10.1029/2003JD004022.
- Jensen, E., et al. (2009), On the importance of small ice crystals in tropical anvil cirrus, *Atmos. Chem. Phys.*, **9**, 5519–5537.
- Jensen, E., G. Diskin, R. P. Lawson, S. Lance, T. P. Bui, D. Hlavka, M. McGill, L. Pfister, O. B. Toon, and R. Gao (2013), Ice nucleation and dehydration in the tropical tropopause layer, *Proc. Natl. Acad. Sci. U.S.A.*, **110**, 2041–2046, doi:10.1073/pnas.1217104110.
- Jiang, J. H., et al. (2010), Five year (2004–2009) observations of upper tropospheric water vapor and cloud ice from MLS and comparisons with GEOS-5 analyses, *J. Geophys. Res.*, **115**, D15103, doi:10.1029/2009JD013256.
- Johnson, D. G., K. W. Jucks, W. A. Traub, and K. V. Chance (2001), Isotopic composition of stratospheric water vapor: Implications for transport, *J. Geophys. Res.*, **106**, 12,219–12,226, doi:10.1029/2000JD900764.
- Kärcher, B., J. Hendricks, and U. Lohmann (2006), Physically based parameterization of cirrus cloud formation for use in global atmospheric models, *J. Geophys. Res.*, **111**, D01205, doi:10.1029/2005JD006219.
- Keith, D. W. (2000), Stratosphere-troposphere exchange: Inferences from the isotopic composition of water vapor, *J. Geophys. Res.*, **105**, 15,167–15,173, doi:10.1029/2000JD900130.
- Kelly, K. K., M. H. Proffitt, K. R. Chan, M. Loewenstein, J. R. Podolske, S. E. Strahan, J. C. Wilson, and D. Kley (1993), Water vapor and cloud water measurements over Darwin during the STEP 1987 tropical mission, *J. Geophys. Res.*, **98**, 8713–8723, doi:10.1029/92JD02526.
- Kim, J.-E., and M. J. Alexander (2013), A new wave scheme for trajectory simulations of stratospheric water vapor, *Geophys. Res. Lett.*, **40**, 5286–5290, doi:10.1002/grl.50963.
- Kley, D., A. L. Schmeltekopf, K. Kelly, R. H. Winkler, T. L. Thompson, and M. McFarland (1982), Transport of water through the tropical tropopause, *Geophys. Res. Lett.*, **9**, 617–620, doi:10.1029/GL009i006p00617.
- Knollenberg, R. G., K. Kelley, and J. C. Wilson (1993), Measurements of high number densities of ice crystals in the tops of tropical cumulonimbus, *J. Geophys. Res.*, **98**, 8639–8664.
- Koop, T., B. Luo, A. Tsias, and T. Peter (2000), Water activity as the determinant for homogeneous ice nucleation in aqueous solutions, *Nature*, **406**, 611–614.
- Lelieveld, J., et al. (2007), Stratospheric dryness: Model simulations and satellite observations, *Atmos. Chem. Phys.*, **7**, 1313–1332.
- Liu, C., and E. J. Zipser (2005), Global distribution of convection penetrating the tropical tropopause, *J. Geophys. Res.*, **110**, D23104, doi:10.1029/2005JD006063.
- Liu, Z., M. Vaughan, D. Winker, C. Kittaka, B. Getzewich, R. Kuehn, A. Omar, K. Powell, C. Trepte, and C. Hostetler (2009), The CALIPSO lidar cloud and aerosol discrimination: Version 2 algorithm and initial assessment of performance, *J. Atmos. Oceanic Technol.*, **26**, 1198–1213, doi:10.1175/2009JTECHA1229.1.
- Locatelli, J. D., and P. V. Hobbs (1974), Fall speeds and masses of solid precipitation particles, *J. Geophys. Res.*, **79**, 2185–2197, doi:10.1029/JC079i015p02185.
- Massie, S., R. Khosravi, and J. C. Gille (2013), A multi-decadal study of cirrus in the tropical tropopause layer, *J. Geophys. Res. Atmos.*, **118**, 7938–7947, doi:10.1002/jgrd.50596.
- McFarquhar, G. M., J. Um, M. Freer, D. Baumgardner, G. L. Kok, and G. Mace (2007), The importance of small ice crystals to cirrus properties: Observations from the Tropical Warm Pool International cloud Experiment (TWP-ICE), *Geophys. Res. Lett.*, **34**, L13803, doi:10.1029/2007GL029865.
- Moorthi, S., and M. J. Suarez (1992), Relaxed Arakawa-Schubert: A parameterization of moist convection for general-circulation models, *Mon. Weather Rev.*, **120**, 978–1002.
- Mote, P. W., K. H. Rosenlof, M. E. McIntyre, E. S. Carr, J. C. Gille, J. R. Holton, J. S. Kinnersley, H. C. Pumphrey, J. M. Russell III, and J. W. Waters (1996), An atmospheric tape recorder: The imprint of tropical tropopause temperatures on stratospheric water vapor, *J. Geophys. Res.*, **101**, 3989–4006, doi:10.1029/95JD03422.

- Moyer, E. J., F. W. Irion, Y. L. Yung, and M. R. Gunson (1996), ATMOS stratospheric deuterated water and implications for troposphere-stratosphere transport, *Geophys. Res. Lett.*, 23, 2385–2388, doi:10.1029/96GL01489.
- Pfister, L., et al. (2001), Aircraft observations of thin cirrus clouds near the tropical tropopause, *J. Geophys. Res.*, 106, 9765–9786, doi:10.1029/2000JD900648.
- Randel, W. J., and E. J. Jensen (2013), Physical processes in the tropical tropopause layer and their role in a changing climate, *Nat. Geosci.*, 6, 169–176, doi:10.1038/ngeo1733.
- Randel, W. J., F. Wu, H. Vömel, G. E. Nedoluha, and P. Forster (2006), Decreases in stratospheric water vapor after 2001: Links to changes in the tropical tropopause and the Brewer-Dobson circulation, *J. Geophys. Res.*, 111, D12312, doi:10.1029/2005JD006744.
- Randel, W. J., M. Park, L. Emmons, D. Kinnison, P. Bernath, K. Walker, C. Boone, and H. Pumphrey (2010), Asian monsoon transport of pollution to the stratosphere, *Science*, 328, 611–613, doi:10.1126/science.1182274.
- Rienecker, M. M., et al. (2011), MERRA: NASA's modern-era retrospective analysis for research and applications, *J. Clim.*, 24, 3624–3648, doi:10.1175/JCLI-D-11-00015.1.
- Riihimaki, L. D., and S. A. McFarlane (2010), Frequency and morphology of tropical tropopause layer cirrus from CALIPSO observations: Are isolated cirrus different from those connected to deep convection?, *J. Geophys. Res.*, 115, D18201, doi:10.1029/2009JD013133.
- Rondanelli, R., and R. S. Lindzen (2010), Can thin cirrus clouds in the tropics provide a solution to the faint young Sun paradox?, *J. Geophys. Res.*, 115, D02108, doi:10.1029/2009JD012050.
- Schiller, C., J.-U. Grooß, P. Konopka, F. Ploger, F. H. Silva dos Santos, and N. Spelten (2009), Hydration and dehydration at the tropical tropopause, *Atmos. Chem. Phys.*, 9, 9647–9660.
- Schoeberl, M. R., and A. E. Dessler (2011), Dehydration of the stratosphere, *Atmos. Chem. Phys.*, 11, 8433–8446, doi:10.5194/acp-11-8433-2011.
- Schoeberl, M. R., et al. (2008), QBO and annual cycle variations in tropical lower stratosphere trace gases from HALOE and Aura MLS observations, *J. Geophys. Res.*, 113, D05301, doi:10.1029/2007JD008678.
- Schoeberl, M. R., A. E. Dessler, and T. Wang (2012), Simulation of stratospheric water vapor and trends using three reanalyses, *Atmos. Chem. Phys. Discuss.*, 12, 8433–8463, doi:10.5194/acpd-12-8433-2012.
- Schoeberl, M. R., A. E. Dessler, and T. Wang (2013), Modeling upper tropospheric and lower stratospheric water vapor anomalies, *Atmos. Chem. Phys. Discuss.*, 13, 9653–9679, doi:10.5194/ACD-13-9653-2013.
- Smith, J. A., A. Ackerman, E. Jensen, and O. B. Toon (2006), Role of deep convection in establishing the isotopic composition of water vapor in the tropical transition layer, *Geophys. Res. Lett.*, 33, L06812, doi:10.1029/2005GL024078.
- Solomon, S., K. H. Rosenlof, R. W. Portmann, J. S. Daniel, S. M. Davis, T. J. Sanford, and G.-K. Plattner (2010), Contributions of stratospheric water vapor to decadal changes in the rate of global warming, *Science*, 237, 1219–1223.
- Ueyama, R., E. J. Jensen, L. Pfister, G. S. Diskin, T. P. Bui, and J. M. Dean-Day (2014), Dehydration in the tropical tropopause layer: A case study for model evaluation using aircraft observations, *J. Geophys. Res. Atmos.*, 119, 5299–5316, doi:10.1002/2013JD021381.
- Vaughan, M., K. Powell, R. Kuehn, S. Young, D. Winker, C. Hostetler, W. Hunt, Z. Liu, M. McGill, and B. Getzewich (2009), Fully automated detection of cloud and aerosol layers in the CALIPSO lidar measurements, *J. Atmos. Oceanic Technol.*, 26, 2034–2050, doi:10.1175/2009JTECHA1228.1.
- Waliser, D., et al. (2009), Cloud ice: A climate model challenge with signs and expectations of progress, *J. Geophys. Res.*, 114, D00A21, doi:10.1029/2008JD010015.
- Wang, P.-H., P. Minnis, M. P. McCormick, G. S. Kent, and K. M. Skeens (1996), A 6-year climatology of cloud occurrence frequency from Stratospheric Aerosol and Gas Experiment II observations (1985–1990), *J. Geophys. Res.*, 101, 29,407–29,429, doi:10.1029/96JD01780.
- Wang, T., and A. E. Dessler (2012), Analysis of cirrus in the tropical tropopause layer from CALIPSO and MLS data: A water perspective, *J. Geophys. Res.*, 117, D04211, doi:10.1029/2011JD016442.
- Wang, T., W. J. Randel, A. E. Dessler, M. R. Schoeberl, and D. E. Kinnison (2014a), Trajectory model simulations of ozone ( $O_3$ ) and carbon monoxide (CO) in the lower stratosphere, *Atmos. Chem. Phys.*, 14, 7135–7147, doi:10.5194/acp-14-7135-2014.
- Wang, T., A. E. Dessler, M. R. Schoeberl, W. J. Randel, and J.-E. Kim (2014b), The impact of temperature resolution on trajectory modeling of stratospheric water vapour, *Atmos. Chem. Phys. Discuss.*, 14, 29,209–29,236, doi:10.5194/acpd-14-29209-2014.
- Winker, D., and C. Trepte (1998), Laminar cirrus observed near the tropical tropopause by LITE, *Geophys. Res. Lett.*, 25, 3351–3354, doi:10.1029/98GL01292.
- Winker, D. M., et al. (2010), The CALIPSO mission: A global 3D view of aerosols and clouds, *Bull. Am. Meteorol. Soc.*, 91, 1211–1229, doi:10.1175/2010BAMS3009.1.
- Wu, D. L., et al. (2009), Comparisons of global cloud ice from MLS, CloudSat, and correlative data sets, *J. Geophys. Res.*, 114, D00A24, doi:10.1029/2008JD009946.
- Wu, D. L., A. Lambert, W. Read, P. Eriksson, and J. Gong (2013), MLS and CALIOP cloud ice measurements in the upper troposphere: A constraint from microwave on cloud microphysics, *J. Appl. Meteorol. Climatol.*, 53, 157–165, doi:10.1175/JAMC-D-13-0411.
- Young, S. A., and M. A. Vaughan (2009), The retrieval of profiles of particulate extinction from Cloud-Aerosol Lidar Infrared Pathfinder Satellite Observations (CALIPSO) data: Algorithm description, *J. Atmos. Oceanic Technol.*, 26, 1105–1119, doi:10.1175/2008JTECHA1221.1.